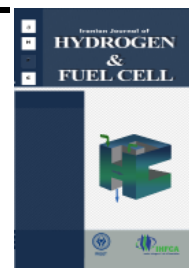


Iranian Journal of Hydrogen & Fuel Cell

IJHFC

Journal homepage://ijhfc.irost.ir



The Impact of Wettability on Effective Properties of the Cathode Catalyst Layer in a Proton Exchange Membrane Fuel Cell

H. Fathi^{1,*}, S. H. Mansouri¹, A. Raof²

¹Department of Mechanical Engineering, Shahid Bahonar University of Kerman, Kerman, Iran

²Department of Earth Sciences, Utrecht University, Utrecht, Netherlands

Article Information

Article History:

Received:

16 Nov 2016

Received in revised form:

18 Dec 2016

Accepted:

26 Dec 2016

Keywords

PEM fuel cell

Cathode catalyst layer

Two-phase flow

Contact angle

Effective diffusivity

Abstract

The produced liquid water in the cathode catalyst layer (CCL) has a significant effect on the operation of a proton exchange membrane fuel cell (PEMFC). To investigate this effect, the transport of oxygen in the CCL in the presence of immiscible liquid water is studied by applying a two-dimensional pore scale model. The CCL was reconstructed as an agglomerated system. To explore the wettability effects, different contact angles were considered at the surface of agglomerates. The effective diffusivity of oxygen was calculated under different contact angles at various saturation levels. The same effective diffusivity was obtained for hydrophilic and hydrophobic domains at lower saturations; however, at saturation above 0.4, the hydrophobic domain provided higher effective diffusivity values. The effect of water coverage at reaction surface areas was investigated. The results showed that, at a saturation of 0.4, the hydrophobic domain with the contact angle of 150 has about 2 times more available surface area due to a different distribution of the water phase compared to the hydrophilic domain with a contact angle of 20.

1. Introduction

Proton exchange membrane fuel cells (PEMFCs) show a great potential to replace internal combustion engines, Lithium-ion batteries in mobile systems, and many other portable power suppliers [1]. They have high-energy density at low operating temperatures

and quick start-up while having zero emissions. To be competitive with traditional energy convertors, PEMFCs should have higher performance and lower losses [2, 3]. It is now clear that the major losses in PEMFCs are happening within the cathode catalyst layer (CCL), where the liquid water is produced [4]. The liquid water, as the product of electrochemical

reactions, floods the pore spaces of the CCL to block the reaction sites, which are the three-phase regions composed of carbon covered by platinum particles, oxygen, and ionomer.

Several studies have been performed on the performance of PEMFC that neglected the presence of water as an immiscible liquid phase in the CCL [5, 6], which is not an evaluated assumption. Some studies have applied various ways to include the presence of liquid water in the CCL, these can be categorized into two groups. The first group assume a priori homogenous distribution of water [7-9] and consider oxygen dissolution through this phase by applying Henry's law [10] or oxygen diffusion through the partially saturated domain using Bruggeman correlation [11]. For example, Bernardi and Verbrugge [12] investigated the presence of liquid water in the CCL to calculate dissolution of oxygen in ionomer. Marr and Li [13] considered the ionomer layer surrounding the catalyst particles to be fully-hydrated, and the void region in the catalyst layer to be fully-flooded. They assumed the dissolved oxygen diffuses through the liquid water first, then through the thin ionomer, surrounding the catalyst particles, before reaching the reaction sites. Following the study of Mar and Li [13], Baschuk and Li [14] used the same formulation and calculated the flux of oxygen for different levels of water flooding in the CCL and its effect on the diffusivity of oxygen applying Bruggeman correlation.

In studies involved in the first group, no distribution of the water phase based on two-phase transport of water on oxygen diffusion was considered. Many other studies applied two-phase flow models to investigate the liquid water transport in PEMFC. Several two-phase modelings of a PEMFC in continuum scale can be found in the literature [15-18]. For example, You and Liu [17] assumed a threshold current density to solve the two-phase flow equations to obtain the distribution of water saturation in the gas diffuser and the gas channel simultaneously; however, not in the CCL as a separate layer. Das et al. [18] developed a one-dimensional analytical solution of water transport across the CCL. Their investigation

of the liquid water production from the phase change process is negligible compared to the production from the electrochemical process. In spite of the mentioned studies in continuum scale, accurate pore scale models are needed to investigate the effect of pore sizes and the configuration of agglomerates in CCL on the performance of fuel cell.

To directly include the pore scale processes in CCL modelling, some studies have applied pore network modelling (PNM) to explore two-phase flow conditions in the catalyst layer by assuming an initial occurrence of the liquid water within the pore spaces [19-22]. For example, El Hannach et al. [19] developed a PNM approach to study two-phase transport phenomena inside a porous structure representative of hydrophilic and hydrophobic CCLs. The electrochemical reactions were not included. They found that the total liquid saturation at the end of water invasion is lower when the pore network is hydrophobic. Since a pore network model uses local rules, in particular for trapping and snap off processes, and applies simple geometries for complex and angular pore structures, more accurate representations of the pore spaces is needed to investigate fluid transports in CCL.

Mukherjee et al. [20] reconstructed the CCL microstructure at the pore scale and used the two-phase S-CLBM to study the liquid water site coverage and pore blockage effects in a reconstructed catalyst layer microstructure and evaluated the relative permeability relation as a function of liquid water saturation. However, they neglected electrochemical reactions, the effect of hydrophobicity or hydrophilicity of the CCL, and the interface effect on consumption and diffusion of oxygen. To the best of the authors' knowledge, there is a lack of pore scale study on the partially-saturated effects on effective diffusivity as well as its effect on changing the available reaction surface area under different degrees of wettability of the CCL. Hutzenlaub et al. [22] investigated the effect of liquid water existence on oxygen diffusion and on specific reaction surface area in a hydrophilic and hydrophobic reconstructed CCL. To apply the water

phase, they made a simplifying assumption that water will occupy the pores from the smallest pore to the largest for the hydrophilic domain and vice versa for the hydrophobic domain preventing the need to solve a two-phase flow problem. The electrochemical reactions and two-phase flow were not considered in their study and they assumed CCL to be either extremely hydrophilic or hydrophobic which is an over-estimation of real CCL behavior.

The distribution of liquid water in a hydrophilic or a hydrophobic porous media depends on how liquid spreads on a solid surface, is controlled by the contact angle, as well as pore filling processes affected by capillary forces. Fig. 1.a shows two different formation of water on the surface of agglomerates with different contact angles. A different arrangement of water on the agglomerates compels different water distributions in the CCL which may have considerable effect on effective diffusivity and on available reactive surface areas for electrochemical reactions.

There are some experimental studies investigating the effect of the CCL with different distributions of poly tetrafluoro ethylene (PTFE) on the performance of PEMFC [23]. The presence of PTFE in the CCL increases the contact angle to warrant hydrophobicity effects. Nam and Kaviani [24] reported that the intrinsic contact angle of PTFE to be about 108 and that the apparent contact angle of the CCL would be 120-140. A numerical study is required to obtain the effect of different contact angles in the CCL which cannot be readily investigated applying experiments. Such knowledge can be utilized in the process of CCL production with increased performance.

In this paper, we performed a two-dimensional pore scale model to investigate the oxygen and liquid water transport in the CCL. The liquid water was assumed to be produced at the surface of the agglomerates, where the small thickness of the ionomer layer has negligible effect on oxygen diffusion [25] and reactions happen mostly at larger (secondary) pores. The produced water was assumed to be present at a reaction zone. Solving two-phase flow equations in the CCL at the pore scale we obtained, for the first

time, the distribution of produced liquid water in the CCL applying different contact angles. For different water saturations, we calculated the effective diffusivity and the available surface area that are not covered by liquid water. Based on our simulations, we have reported an optimum contact angle resulting in the maximum performance of the CCL.

2. Methodology

A CCL is constructed of agglomerates of carbon particles covered by platinum particles and connected to each other by the ionomer phase (a hydrophilic electrolyte). Addition of PTFE imposes hydrophobic conditions in the pore spaces. Oxygen, ionomer, and carbon covered by platinum particles make a three-phase region over which the electrochemical reactions occur. Oxygen in the CCL diffuses through the pore spaces to reach the reaction sites. The product of electrochemical reactions, mostly liquid water, creates a barrier against oxygen transport to reach the three-phase region.

To create a two-dimensional pore structure of the CCL we considered a part of this layer situated close to the gas diffusion layer (GDL) with the size of $5\mu\text{m} \times 5\mu\text{m}$, while the agglomerates were semi-sized circles with the diameter of 500 nm and in random locations [26]. The size of the domain was chosen large enough to minimize differences between different realizations [25].

2.1. Volume of Fluid Method

To obtain the distribution of water in the CCL, two equations were solved: a momentum equation that includes surface tension force, and a continuity equation. The momentum equation may be written as:

$$\frac{\partial(\rho U)}{\partial t} + \nabla \cdot (\rho U U) - \nabla \cdot (\mu \nabla U) - \rho g = -\nabla p - F_s \quad (1)$$

Here ρ is fluid density, U is the local fluid velocity, t is the time, μ is the viscosity, p is the local pressure, and F_s is the surface tension force, which is applied

at moving phase interfaces. Flow of the liquid water was simulated by applying the volume of fluid (VOF) method. Ability of the VOF method to model micro- and nanoscale processes was shown by Bedram and Moosavi [27] who investigated the breakup of droplets and verified the results against experimental and analytical values. Momentum and continuity equations were solved in order to obtain the liquid phase volume (F_v) in each cell of the imposed numerical grid, such that $F_v = \alpha V_{cell}$, where V_{cell} is the cell volume. The value of α will be one and zero for completely saturated and dry cells, respectively, and between zero and one at phase interfaces [28]. The movement of interfaces is calculated by solving a transport equation for α as:

$$\frac{\partial \alpha}{\partial t} + \nabla \cdot (U\alpha) + \nabla \cdot (\alpha(1-\alpha)U_r) = 0 \quad (2)$$

in which

$$U_r = c_r |U| \frac{\nabla \alpha}{|\nabla \alpha|}$$

The last term of Equation (2) is applied at the interface. This term represents a compression term as suggested by Weller [29] in order to minimize dispersion of the interface. The parameter c_r controls the compression of the interface. Following Weller [29], the value of c_r was taken within the range of $1 \leq c_r \leq 4$ in order to obtain a sharp interface. The physical properties of a numerical cell were calculated as weighted averages using the volume fraction, α , of the two fluids occupying the cell. The fluid density at any point within the domain is then given by:

$$\rho = \alpha \rho_w + (1-\alpha) \rho_a \quad (3)$$

where ρ_w and ρ_a are the densities of water and air, respectively. The viscosity, μ , is calculated in a similar way. The surface tension force, F_s , in Equation (1) can be obtained as:

$$F_s = \sigma \kappa(x) \mathbf{n} \quad (4)$$

where σ is the surface tension of water in contact with air, \mathbf{n} is a unit vector normal to the interface, defined as:

$$\mathbf{n} = \frac{\nabla \alpha}{|\nabla \alpha|} \quad (5)$$

and κ is the curvature of the interface, which is obtained using

$$\kappa(x) = \nabla \cdot \mathbf{n} \quad (6)$$

2.2. Simulation procedure

The discretized form of governing equations was solved using OPENFOAM software [30] applying the finite volume method. Each local numerical cell was considered as water saturated when the molar ratio of liquid water (volume fraction, α) in that cell became one. Fig. 1.b provides a schematic part of the numerical domain used in our simulation, showing that cells adjacent to the surfaces of agglomerates form the reaction zones to produce water.

Solving the two-phase flow at each time step of water production is extremely time consuming. As such, we have applied a semi-dynamic approach using the cells in the reaction zone which were assigned as water saturated, the two-phase flow equations were then solved to obtain the updated distribution of liquid water. The α value of all cells at the reaction zone was changed to one when the two-phase flow solution at each step reached the steady-state condition. Fig. 2 shows the algorithm applied for this numerical procedure. In the two-phase flow simulation, we assumed the surface of the agglomerates as solid surfaces with specific contact angles and the symmetry condition was applied for the rest of boundaries.

2.3. Applying the wettability effect

To explore the wettability effects on performance of the CCL several simulations applying different contact angles at the surface of agglomerates were performed, which is a boundary condition to solve Equation (2). This boundary condition has been

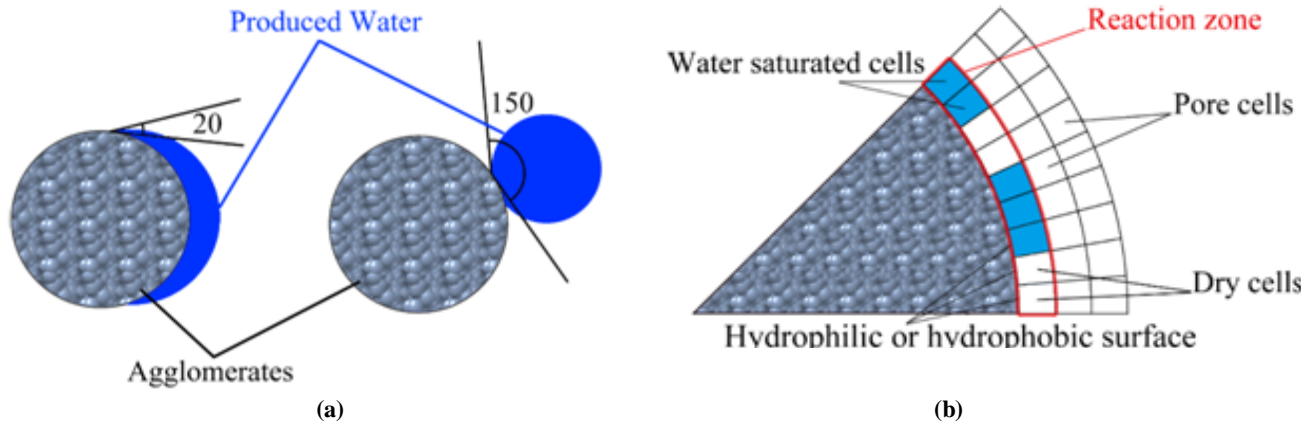


Fig. 1. a) The effect of contact angle on water formation at the surface of agglomerates. b) A schema of the cells applied in the numerical procedure.

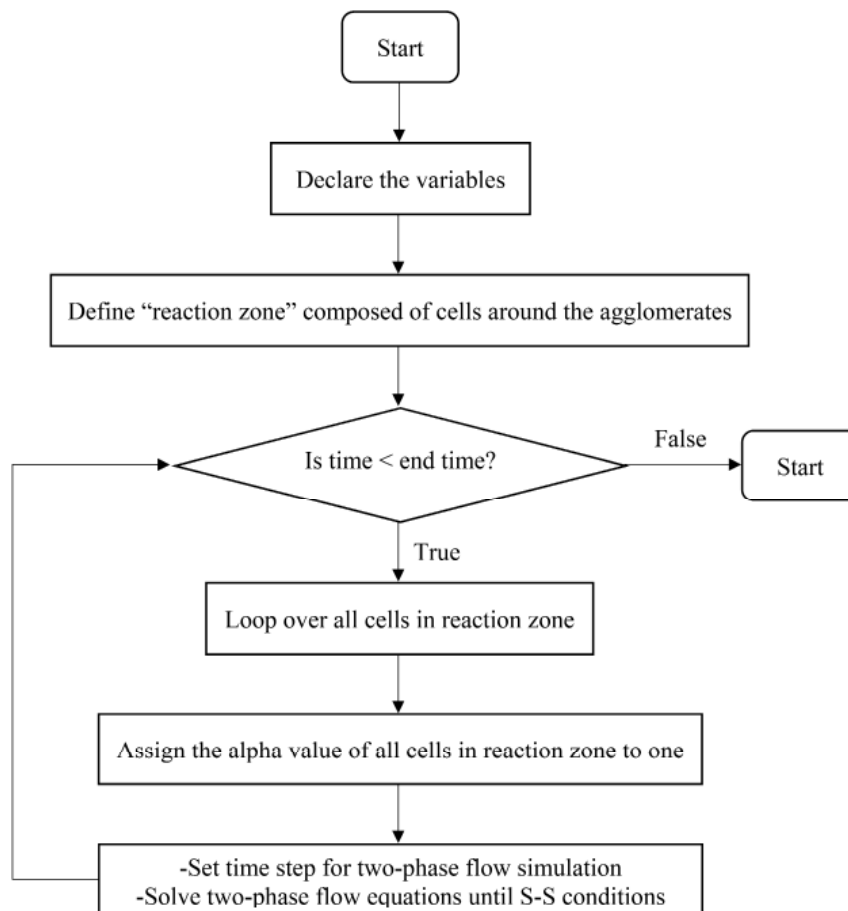


Fig. 2. Flowchart of the numerical procedure.

defined in the interFoam solver of OpenFOAM software through which a fixed value for a contact angle can be assigned at the surface of the agglomerates. Based on the value of the contact angle, the distribution of α value at the cells adjacent

to the surfaces of the agglomerates is determined. While a value of contact angle below 90 makes the surface hydrophilic, a value larger than 90 creates a hydrophobic surface (Fig. 1.a). Wettability changes have a distinctly different effect on the resulting

water distribution in the CCL that is composed of pores with different sizes. Under hydrophobic conditions, water is being transported to the larger pores and results in blocking of oxygen pathways through these pores to decrease diffusive flux of oxygen into the porous media. At the same time, hydrophobicity will cause water to cover less of the reactive surface areas at the agglomerates where electrochemical reactions may occur. In contrast, under hydrophilic conditions water is moved into the smaller pores and keeps larger pores dry where oxygen can diffuse. However, hydrophilic surfaces increase wettability and cause a larger fraction of the reactive surface areas to be covered by liquid water. Therefore, different degrees of wettability have a profound effect on CCL performance.

2.4. Effective Diffusivity

We would like to obtain the value of effective diffusivity (i.e., the integrated diffusivity of the whole domain) under different water saturation. To do so, we have taken the resulting air and water distributions and applied a tracer (oxygen) transport through the domain at several stages having different saturation levels during the two-phase reactive transport. Having the distribution of air and water in domain, the concentration of tracer was fixed at the inlet and the opposite interface. The transport equations for oxygen in air and water in a variable saturated domain are as follows, respectively:

$$\nabla \cdot ((1-S)D_{O_2}^a (\nabla X_{O_2}^a)) = 0 \quad (7)$$

$$\nabla \cdot (SD_{O_2}^w (\nabla X_{O_2}^w)) = 0 \quad (8)$$

In Equations (7) and (8), $X_{O_2}^a$ and $X_{O_2}^w$ are oxygen concentrations in air and water, respectively, S is the local volume fraction of water, and $D_{O_2}^a$ and $D_{O_2}^w$ are the diffusion coefficients of oxygen in air and water, respectively. Combining Equations (7) and (8), a single transport equation was solved as follows to obtain the flux of oxygen across the whole domain:

$$\nabla \cdot (SD_{O_2}^w (\nabla X_{O_2}^w)) + \nabla \cdot ((1-S)D_{O_2}^a (\nabla X_{O_2}^a)) = 0 \quad (9)$$

The concentration field is continuous and Henry's law may be applied to the couple oxygen concentration in the air and water phases at the air-water interface as:

$$X_{O_2}^a = H_{O_2}^{cc} X_{O_2}^w \quad (10)$$

where $H_{O_2}^{cc}$ is the Henry's solubility constant. As pore length scales in the CCL are typically nano scale, the oxygen diffusivity is calculated by taking into account the contribution of binary oxygen diffusivity in air, D_{O_2-a} as well as the Knudsen diffusivity, $D_{O_2,Kn}$. The Knudsen diffusivity can be obtained as [31]:

$$D_{O_2,Kn} = \frac{d_p}{3} \sqrt{\frac{8RT}{\pi M_{O_2}}} \quad (11)$$

where d_p is the pore diameter, R is the universal gas constant, T is the local temperature, and M_{O_2} is the molecular weight of oxygen. In this study, we used the average pore diameter for d_p in Equation (11) [25]. The effective, local scale oxygen diffusivity in air, $D_{O_2}^a$, is obtained using the Bosanquet equation [32] as:

$$D_{O_2}^a = \left(\frac{1}{D_{O_2-a}} + \frac{1}{D_{O_2,Kn}} \right)^{-1} \quad (12)$$

Next, the calculated flux of oxygen at the outlet, Γ_{out} , was used to obtain the dimensionless effective diffusivity, D , using:

$$D = \frac{\Gamma_{out} L}{D_{O_2-a} A (X_1 - X_2)} \quad (13)$$

which has been normalized by D_{O_2-a} . In Equation (13), X_1 and X_2 are the applied tracer molar ratios at the inlet and outlet boundaries, L is the total length of the domain which is equal to 5 μm and A is the cross sectional area of the bounding box of the domain. Table 1 shows the values of parameters used in this study.

3. Results and Discussion

3.1. Model Validation

Simulation results of diffusivity are often validated

Table 1. Parameters and their values used in simulations

Property	Value
Temperature, T (K)	353
Pressure, P (atm)	1.5
Universal gas constant, R ($J.mol^{-1}.K^{-1}$)	8.314
Agglomerate diameter (nm)	500
D_{O_2-a} ($cm^2.s^{-1}$)	0.1769 [33]
$D_{O_2}^w$ ($cm^2.s^{-1}$)	6.395×10^{-5} [34]
$H_{O_2}^{cc}$	42.785 [35]

d against the results from the Bruggeman correlation. The Bruggeman relation [11] describes tortuosity, τ , as $\tau = \varepsilon^{1/2}$, where ε is the porosity. Tortuosity may be correlated to the normalized effective diffusivity, D , through the expression $D = \varepsilon/\tau$ [36]. Substituting the Bruggeman relation into the effective diffusivity expression provides $D = \varepsilon^{3/2}$. This equation is known as Bruggeman correlation for effective diffusivity [25]. Moreover, Bruggeman conducted several experiments using a porous domain composed of uniformly spaced, equally-sized, solid spheres [11]. The porosity of such a media can be estimated as $(1 - \pi/6)$, regardless of sphere diameters. These conditions lead to $D = (1 - \pi/6)^{3/2} \approx 0.3288$. To validate the model accuracy, we solved the oxygen transport equation (Equation (9)) for a three-dimensional domain consisting of 125 equally-sized spheres which are uniformly located in a cube similar to the Bruggeman experiments. The effective diffusivity for such a domain was obtained as 0.3228 which is in good agreement with the Bruggeman correlation. The slight difference may be due to the use of structured mesh which results in less accuracy in representing circular surfaces. Since the Bruggeman experiments were performed in three-dimensions, the simulations for comparison were made for a three-dimensional domain. However, due to the tremendous computational complexities during pore-scale multi-phase flow, it is common to apply two-dimensional pore structures. Therefore, we decided to solve the governing equations in a two-dimensional domain as has been done by several other studies [37-41].

3.2. Two-Phase Flow Simulation

The distribution of the produced liquid water was obtained for different water saturations in the domain with a porosity of 0.50. Fig. 3 provides water distribution in hydrophilic and hydrophobic domains under different saturation levels. At lower saturation levels, larger pores are the main pathway for diffusion of oxygen. Water is being transported into the larger pores when the domain is hydrophobic. Therefore, compared to the hydrophobic domain, diffusion of oxygen in a hydrophilic domain is larger at lower saturation levels. However, in contrast, at higher saturation, the larger pores are filled with water while the smaller pores provide a pathway for oxygen diffusion. Therefore, the diffusivity of hydrophobic domain, which has higher fraction of air-filled small pores, dominates at lower saturations (unfilled circles in Fig. 3.c and 3.g).

Due to the presence of nano-pores in the CCL, the capillary forces are huge (the capillary number is less than 10^{-5} [20]) which results in large amounts of velocities at the air/water interfaces, initially. The velocity distributions in the CCL with contact angles of 20 and 150 are shown in Figures 4a and 4c, respectively. Both domains are under the saturation of 0.5 and the water distributions are shown in Fig. 4.b and 4.d. The large amounts of velocities at the air/water interfaces lead water to quickly reach its final distribution at each step (described in Section 2.2). This is the reason for observing a permanent quasi-static two-phase flow in the CCL by Ref. [42]. To investigate the effect of wettability on the distribution of water, statistically, the pore size distribution in the domain including wet pores are shown in Fig. 5. It can be observed that smaller pores are more occupied in the hydrophilic domain. The reason is the tendency of water to invade the small pores in this domain. Clearly, larger pores are more filled by water in the hydrophobic domain.

3.3. Oxygen Effective Diffusivity

Tracer transport was performed for different

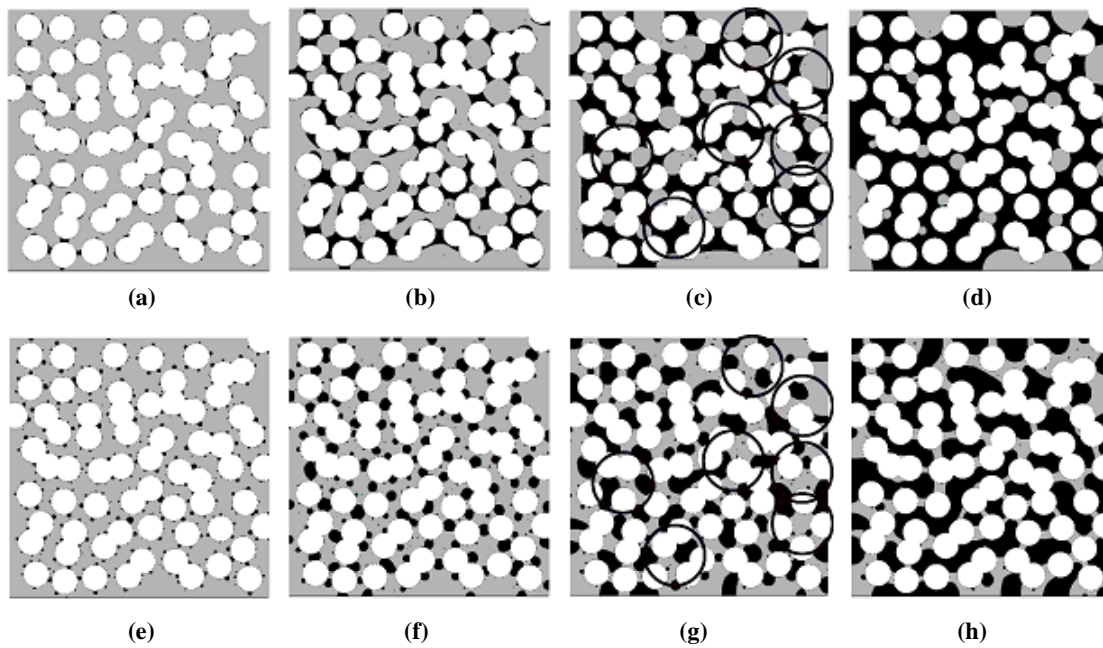


Fig.3. Water distribution for (a) - (d): a hydrophilic domain with the contact angle of 20; and (e) - (h): a hydrophobic domain with the contact angle of 150. Saturation is 0.10 in (a) and (e), 0.30 in (b) and (f), 0.50 in (c) and (g), and 0.70 in (d) and (h). The porosity of the domain is 0.50. The values of α higher than 0.50 were shown for better visibility of liquid water which is in black. The gray area is air and agglomerates are shown in white.

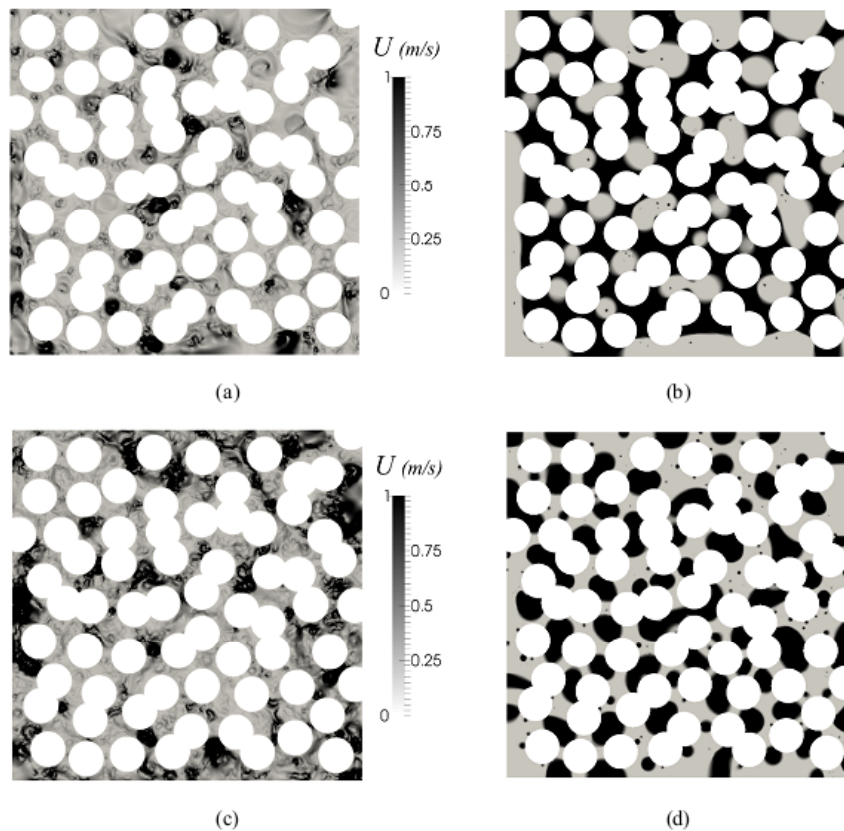


Fig. 4. Velocity and water distributions for: (a) & (b) a hydrophilic domain with the contact angle of 20; and (c) & (d) a hydrophobic domain with the contact angle of 150. Both domains are under the saturation of 0.5. The liquid water in (b) and (d) is shown in black while the air and the agglomerates are shown in gray and white, respectively.

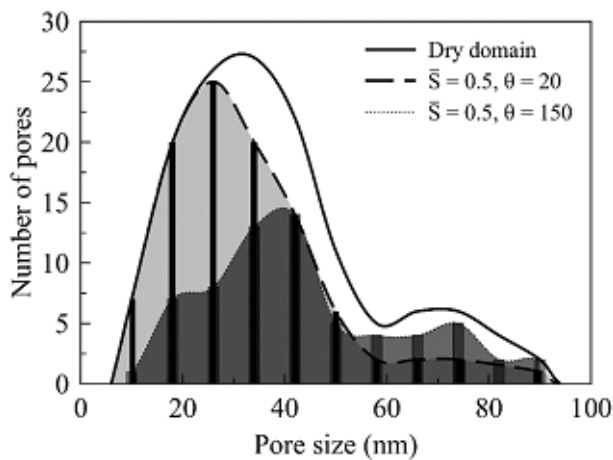


Fig. 5. The pore size distribution of the domain and the saturated pores in hydrophilic and hydrophobic domains. \bar{S} is the average liquid saturation of the domain.

t saturations as well as considering different contact angles. Fig. 6 shows the effect of water content on normalized effective diffusivity. The effective diffusivities of the hydrophilic and hydrophobic domains are relatively equal at the lower saturations, although the hydrophilic domain shows slightly higher effective diffusivity values (Fig. 6.a). This is due to the fact that the hydrophilic domain has more air-filled larger pores at lower saturations through which oxygen can diffuse. At higher saturation, a larger fraction of bigger pores is filled with water in the hydrophobic domain and air-filled small pores (Fig. 3.g) contribute more to oxygen diffusion. In contrast, almost all small pores are

occupied by water at higher saturation levels in the hydrophilic domain which means fewer pore throats are available for oxygen diffusion. Therefore, as expected, the hydrophobic domain has higher effective diffusivity compared to the hydrophilic domain at higher saturation (Fig. 6.b).

The normalized effective diffusivities in the domain with different contact angles were provided in Table 2 for two saturation levels of 0.30 and 0.70. The data shows that, due to the increase of water-filled larger pores, an increasing contact angle in the hydrophilic domain decreases the effective diffusivity at the saturation of 0.30. On the other hand, the presence of air-filled smaller pores enhances effective diffusivity at saturation of 0.70 when the contact angle increases. The effective diffusivity in the hydrophobic domain is increased at the saturation of 0.30 when the contact angle increases. This can be affected by accumulation of water which makes more air-filled pores as the passages of oxygen diffusion. At the saturation of 0.70, the hydrophobic domain with higher contact angle has more air-filled small pores through which oxygen can diffuse, hence an increasing contact angle enhances the effective diffusivity. The same behavior of partially saturated hydrophilic and hydrophobic domains was observed by Hutzenlaub et al. [22].

3.4. Available Surface Area

As mentioned earlier, an undesirable effect due to

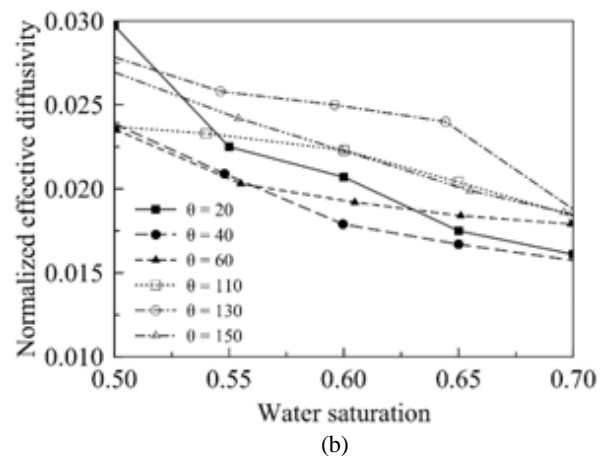
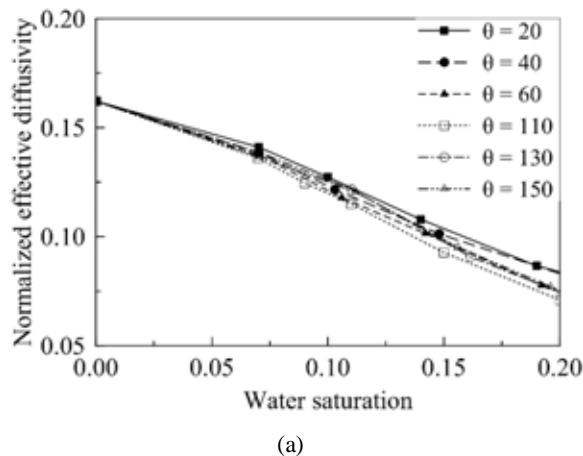


Fig. 6. Normalized effective diffusivity versus water saturation at a) low and b) high saturation levels. Data points have been connected with lines for better visibility.

Table 2. Normalized effective diffusivity for low and high saturations

Contact Angle	D	
Hydrophilic:	$\bar{S}^* = 0.3$	$\bar{S} = 0.7$
20	0.0852	0.0234
40	0.0796	0.0265
60	0.0796	0.0281
Hydrophobic:		
110	0.0697	0.0268
130	0.0777	0.0274
150	0.0893	0.0292

* \bar{S} is the average liquid saturation of the domain.

the presence of water is coverage of reactive surface areas at the surface of agglomerates. We calculated the fraction of dry surface area of agglomerates (Fig.1.b). Fig. 7 shows how the available reactive surface area decreases by increasing saturation level under different contact angles. It is clear that wettability has a profound effect on the evolution of the reactive surface area. For example, at the saturation of 0.40, the hydrophobic domain, with the contact angle of 150, has about a two times larger value of available reactive surface area compared to the hydrophilic domain with the contact angle of 20

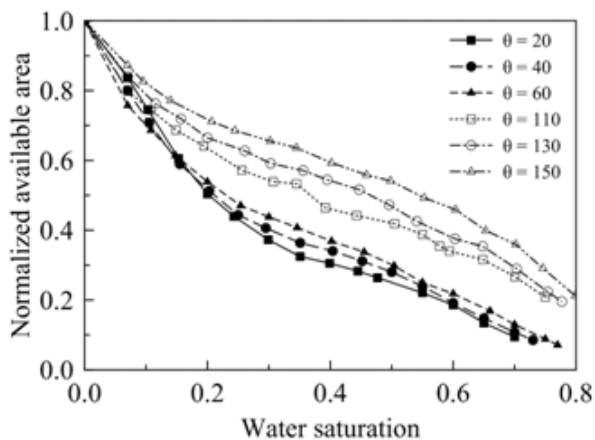


Fig. 7. The covering effect of water saturation on available surface area for different contact angles. Vertical axis shows available surface area which has been normalized by the total surface area of the agglomerates. Data points have been connected with lines for better visibility.

as can be observed in Table 3. Results suggest that a contact angle value around 150 can enhance solute transport to increase performance of the PEMFC.

Table 3. The dry portion of agglomerate surfaces which were not covered by liquid water at the saturation of 0.40

Contact Angle	Dry portion
Hydrophilic:	
20	0.31
40	0.34
60	0.37
Hydrophobic:	
110	0.46
130	0.55
150	0.59

4. Conclusion

Operation of a PEMFC fuel cell generates liquid water the continuation of which affects the performance of the system. This is due to the fact that the produced liquid water, affects both transport processes along the pore spaces of the cathode catalyst layer (CCL) and reaction processes taking place at the solid agglomerate surfaces. Using a pore scale model we have looked into the effect of distributions of the produced water in the CCL considering different contact angles to explore changes of effective diffusivity and available reactive surface area. Applying the semi-dynamic approach,

the liquid water was imported into the reaction zone. The subsequent two-phase flow through the domain was simulated using the volume of fluid method. The simulation was performed for several different contact angles, to cover a wide range of hydrophilic and hydrophobic conditions. The normalized effective diffusivity was obtained for each domain and the results showed that the hydrophilic domain provides higher effective diffusivity at lower saturation due to a larger fraction of larger air-filled pores. At higher saturation, the hydrophobic condition results in higher effective diffusivity as there exist small air-filled pores for oxygen to diffuse through the domain. The coverage of reactive surface areas by liquid water is intense under hydrophilic conditions. Results showed that a domain with the contact angle of 150 has an available surface area two times larger than a domain with the contact angle of 20. In spite of the fact that results of effective diffusivity were underestimated in 2D modelling in comparison with 3D, the behaviour of the system was similar to the results of the 3D model proposed by Hutzenlaub et al. [22]. Results suggest that a contact angle of about 150 provides more available surface area. It should be noted that in order to avoid dehydration of ionomer in the CCL, there is a constraint on the increase of contact angle, which should be further studied.

Nomenclatures

A	Cross sectional area of the bounding box (m^2)
c_r	Factor of interface compression
D	Normalized effective diffusivity
D_{O_2-a}	Oxygen diffusivity in air ($m^2.s^{-1}$)
$D_{O_2}^a$	Oxygen diffusivity in air including Knudsen effect ($m^2.s^{-1}$)
$D_{O_2,Kn}$	Knudsen diffusivity ($m^2.s^{-1}$)
$D_{O_2}^w$	Oxygen diffusivity in water ($m^2.s^{-1}$)
d_p	Pore diameter (m)
F_s	Surface tension force (N)
g	Gravity force (N)
$H_{O_2}^{cc}$	Henry constant
L	Total length of the domain

M_{O_2}	Molecular weight of oxygen ($gr.mol^{-1}$)
n	Unit vector normal to the interface
p	Local pressure (Pa)
R	Universal gas constant ($J.kg^{-1}.K^{-1}$)
S	Local volume fraction of water
\bar{S}	Average liquid saturation
t	Time (s)
T	Temperature (K)
U	Local fluid velocity ($m.s^{-1}$)
U_r	Air/water interface velocity
X_1	Tracer molar ration at the inlet
X_2	Tracer molar ration at the outlet
$X_{O_2}^a$	Oxygen concentration in air ($mol.mol^{-1}$)
$X_{O_2}^w$	Oxygen concentration in water ($mol.mol^{-1}$)

Greek letters

α	Volume fraction
Γ_{out}	Out flux of oxygen ($mol.mol^{-1}.m^3.s^{-1}$)
ε	Porosity
θ	Contact angle
κ	Interface curvature (m^{-1})
μ	Fluid viscosity (Pa.s)
ρ	Fluid density ($kg.m^{-3}$)
ρ_a	Air density ($kg.m^{-3}$)
ρ_w	Water density ($kg.m^{-3}$)
σ	Surface tension of water ($N.m^{-1}$)
τ	Tortuosity

References

- [1] Fuel Cell Technologies Market Report 2015. http://energy.gov/sites/prod/files/2016/10/f33/fcto_2015_market_report.pdf, 2016 (accessed 18.12.16).
- [2] Habibnia M., Shakeri M., Nourouzi S., Tamami, P. G., "Investigation and optimization of a PEM fuel cell's electrical and mechanical behavior", Iranian Journal of Hydrogen & Fuel Cell, 2016, 1: 1.
- [3] Hassanzadeh H. and Golkar S. H., "Modeling and optimization of a non-isothermal two phase flow in the

cathode gas diffusion layer of PEM fuel cell”, *Iranian Journal of Hydrogen & Fuel Cell*, 2015, 3: 159.

[4] Tohidi M., Mansouri S.H., Amiri H., “Effect of primary parameters on the performance of PEM fuel cell”, *Int. J. Hydrogen Energy*, 2010, 35: 9338.

[5] Ticianelli E., Beery J. and Srinivasan S., “Dependence of performance of solid polymer electrolyte fuel cells with low platinum loading on morphologic characteristics of the electrodes”, *J. Appl. Electrochem.*, 1991, 21: 597.

[6] Nguyen T. V. and White R. E., “A water and heat management model for Proton-Exchange-Membrane fuel cells”, *J. Electrochem. Soc.*, 1993, 140: 2178.

[7] Bernardi D. M. and Verbrugge M. W., “Mathematical model of a gas diffusion electrode bonded to a polymer electrolyte”, *AIChE J.*, 1991, 37: 1151.

[8] Wang Q., Eikerling M., Song D. and Liu Z., “Structure and performance of different types of agglomerates in cathode catalyst layers of PEM fuel cells”, *J. Electroanal. Chem.*, 2004, 573: 61.

[9] Khajeh-Hosseini-Dalasm N., Kermani M.J., Moghaddam D.G. and Stockie J.M., “A parametric study of cathode catalyst layer structural parameters on the performance of a PEM fuel cell”, *Int. J. Hydrogen Energy*, 2010, 35: 2417.

[10] Henry W., “Experiments on the quantity of gases absorbed by water, at different temperatures, and under different pressures”, *Phil. Trans. R. Soc. B.*, 1803, 93: 29.

[11] Bruggeman V. D., “Berechnung verschiedener physikalischer Konstanten von heterogenen Substanzen. I. Dielektrizitätskonstanten und Leitfähigkeiten der Mischkörper aus isotropen Substanzen”, *Ann. Phys.*, 1935, 416: 636.

[12] Bernardi D. M., and Verbrugge M. W., “A mathematical model of the solid-polymer-electrolyte fuel cell”, *J. Electrochem. Soc.*, 1992, 139: 2477.

[13] Marr C. and Li X., “Composition and performance modelling of catalyst layer in a proton exchange membrane fuel cell”, *J. Power Sources*, 1999, 77: 17.

[14] Baschuk J. and Li X., “Modelling of polymer electrolyte membrane fuel cells with variable degrees of water flooding”, *J. Power Sources*, 2000, 86: 181.

[15] Gurau V., Liu H. and Kakac S., “Two-dimensional model for proton exchange membrane fuel cells”, *AIChE J.*, 1998, 44: 2410.

[16] Xing L., Mamlouk M., Kumar R. and Scott K., “Numerical investigation of the optimal Nafion® ionomer content in cathode catalyst layer: An agglomerate two-phase flow modelling”, 2014, 39: 9087.

[17] You L. and Liu H., “A two-phase flow and transport model for the cathode of PEM fuel cells”, *Int. J. Heat. Mass Transfer*, 2002, 45: 2277.

[18] Das P. K., Li X. and Liu Z. S., “Analysis of liquid water transport in cathode catalyst layer of PEM fuel cells” *Int. J. Hydrogen Energy*, 2010, 35: 2403.

[19] El Hannach, M., Pauchet J. and Prat M., “Pore network modeling: application to multiphase transport inside the cathode catalyst layer of proton exchange membrane fuel cell”, *Electrochim. Acta*, 2011, 56: 10796.

[20] Mukherjee P. P., and Wang C. Y., “Modeling of catalyst layer surface coverage and volume blockage owing to liquid water in a PEFC”, *ECS. Trans.*, 2010, 3: 1085.

[21] Alink R. and Gerteisen D., “Modeling the liquid water transport in the gas diffusion layer for polymer electrolyte membrane fuel cells using a water path network”, *Energies*, 2013, 6: 4508.

[22] Hutzenlaub T., Becker J., Zengerle R. and Thiele S., “Modelling the water distribution within a hydrophilic and hydrophobic 3D reconstructed cathode catalyst layer of a proton exchange membrane fuel cell”, *J. Power Sources*,

- 2013, 227: 260.
- [23] Uchida M., Aoyama Y., Eda N. and Ohta A., "Investigation of the Microstructure in the Catalyst Layer and Effects of Both Perfluorosulfonate Ionomer and PTFE-Loaded Carbon on the Catalyst Layer of Polymer Electrolyte Fuel Cells", *J. Electrochem. Soc.*, 1995, 142: 4143.
- [24] Nam J. H. and Kaviany M., "Effective diffusivity and water-saturation distribution in single-and two-layer PEMFC diffusion medium", *Int. J. Heat. Mass Transfer.*, 2003, 46: 4595.
- [25] Lange K. J., Sui P. C. and Djilali N., "Pore scale simulation of transport and electrochemical reactions in reconstructed PEMFC catalyst layers", *J. Electrochem. Soc.*, 2010, 157: B1434.
- [26] Dobson P., Lei C., Navessin T. and Secanell M., "Characterization of the PEM fuel cell catalyst layer microstructure by nonlinear least-squares parameter estimation", *J. Electrochem. Soc.*, 2012, 159: B514.
- [27] Bedram, A. and Moosavi, A., "Breakup of Droplets in Micro and Nanofluidic T-Junctions", *J. Appl. Fluid Mech.*, 2013, 6: 81.
- [28] Hirt C. W. and Nichols B. D., "Volume of fluid (VOF) method for the dynamics of free boundaries", *J. Comput. Phys.*, 1981, 39: 201.
- [29] Weller H., "A new approach to VOF-based interface capturing methods for incompressible and compressible flow", OpenCFD Ltd, Report TR/HGW/04, 2008.
- [30] The OpenFOAM Foundation, <http://www.openfoam.org/>, 2016, (accessed 14.08.16).
- [31] Mason EA, Malinauskas A. Gas transport in porous media: the dusty-gas model: Elsevier Science Ltd; 1983.
- [32] Bosanquet C., British TA Report BR-507, Sep. 1944.
- [33] Fuller E. N., Schettler P. D. and Giddings J. C., "New method for prediction of binary gas-phase diffusion coefficients", *Ind. Eng. Chem.*, 1966, 58: 18.
- [34] Hayduk W. and Laudie H., "Prediction of diffusion coefficients for nonelectrolytes in dilute aqueous solutions", *AIChE J.*, 1974, 20: 611.
- [35] Amphlett J. C., Baumert R., Mann R. F., Peppley B. A., Roberge P. R. and Harris T. J., "Performance modeling of the Ballard Mark IV solid polymer electrolyte fuel cell I. Mechanistic model development", *J. Electrochem. Soc.*, 1995, 142: 1.
- [36] Petersen E. E., "Diffusion in a pore of varying cross section", *AIChE J.*, 1958, 4: 343.
- [37] Aker E., Måløy K. J., Hansen A., and Batrouni G. G., "A two-dimensional network simulator for two-phase flow in porous media", *Transport. Porous. Med.*, 1998, 32 (2): 163.
- [38] Lv M. and Wang S., "Pore-scale modeling of a water/oil two-phase flow in hot water flooding for enhanced oil recovery", *RSC Advances*, 2015, 5 (104): 85373.
- [39] Shao Z. S., "Two-dimensional hydrodynamic modeling of two-phase flow for understanding geyser phenomena in urban stormwater system", Ph.D. Thesis, Uni. Kent., US., 2013.
- [40] Santiago C., Ghomeshi S., Kryuchkov Bryan S., J., and Kantzas A., "Pore-Scale Simulations of Haines Jumps during Two-Phase Flow in Porous Media", *GeoConvention*, 2015.
- [41] Ferrari A., Jimenez-Martinez J., Borgne T. L., Méheust Y., and Lunati I., "Challenges in modeling unstable two-phase flow experiments in porous micromodels", *Water Resour. Res.*, 2015, 51 (3): 1381.
- [42] Yu H.M., Ziegler C., Oszcipok M., Zobel M. and Hebling C., "Hydrophilicity and hydrophobicity study of catalyst layers in proton exchange membrane fuel cells", *Electrochim. Acta*, 2006, 51: 1199.